PHYSICAL REVIEW B **106**, 045128 (2022)

# Evolution of geometric and electronic structures of oxygen-induced superstructures on Mo(110) surface: A LEED, ARPES, and DFT study

Arunava Kar,[1] Arpan Das,[2] Smruti Ranjan Mohanty,[1] Shobhana Narasimhan,[2] and Krishnakumar S. R. Menon[1,*]
[1]*Surface Physics and Material Science Division, Saha Institute of Nuclear Physics, A CI of Homi Bhabha National Institute, 1/AF Bidhannagar, Kolkata 700064, India*
[2]*Theoretical Sciences Unit, Jawaharlal Nehru Centre for Advanced Scientific Research, Jakkur, Bangalore 560064, India*

(Received 6 June 2022; revised 29 June 2022; accepted 6 July 2022; published 21 July 2022)

We have studied the evolution of atomic structure and electronic band dispersion of oxygen-induced superstructures on the Mo(110) surface by using low-energy electron diffraction, angle-resolved photoemission spectroscopy, and density functional theory. Our experiments show that adsorption of oxygen at an elevated temperature (473 K) gets rid of the mixed-phase coexisting region observed at room temperature and exhibits three distinct superstructures: $p(2\times2)$, $p(2\times1)$, and $p(2\times6)$ phases. Oxygenation of the Mo(110) surface leads to a confinement-induced gaplike opening at the zone center that can be tuned by the overlayer oxygen coverage. The "hole" pockets on the Fermi surface of the clean Mo(110) surface are found to persist upon oxygen adsorption with slightly changed volumes, while the "electron" pocket does not show any significant shift in momentum with no Fermi surface nesting behavior until saturation oxygen coverages. Apart from the significant modifications to the electronic states of the clean Mo(110) surface, we also observe the formation of new oxygen-induced bands. The evolution of the surface states near $E_F$ can be attributed to a change in the surface potential, while the evolution of oxygen-induced bands results from the hybridization between O-2$p$ ($m_j = 1/2$) and Mo-4$d$ ($m_j = 1/2$) orbitals at the interface. The interlayer separation, bond length, and lateral repulsive interactions between the adatoms are found to play a crucial role in the selective chemisorption of the Mo(110) surface.

DOI: 10.1103/PhysRevB.106.045128

## I. INTRODUCTION

Understanding the adsorption of oxygen and the formation of oxide layers on metal surfaces plays an important role in the development of materials science and engineering. While molybdenum is a heavily used refractive metal, its oxides also find applications in various fields such as catalytic activities, gas sensors, various chemical reactions, $H_2$ generation, supercapacitors, and lithium-ion batteries [1–5]. The initial oxidation stages of the Mo(110) surface have been investigated since the beginning of modern surface science [6–12]. Using low-energy electron diffraction (LEED) and Auger electron spectroscopy, Witt and Bauer [6] established a phase diagram of coverage-dependent oxygen-induced structures on the Mo(110) surface for room-temperature (RT) adsorption. For an oxygen surface coverage of 0.25 monolayer (ML), they observed a $p(2\times2)$ superstructure on Mo(110) for RT adsorption while complex surface structures were observed for larger coverages ($\geqslant 0.3$ ML). Heating the ordered $p(2\times2)$ phase higher than 700 K exhibits a $(1\times1)$ disorder continuous phase transition, whereas at lower temperature there exists a tricritical point and a first-order phase transition [6,13]. However, only a few experimental studies have been reported for oxygen adsorption of Mo(110) surfaces for temperatures below 750 K, due to either the observation of complex surface structures or the lack of observable surface reconstructions.

Exposing the clean Mo(110) surface to high oxygen partial pressures of $\sim10^{-6}$ mbar at 1273 K forms $MoO_2$ with a complicated surface structure [14], while heating the sample with an adsorbed oxygen layer does not form the oxide layer. Furthermore, studies have shown that for the oxide layer formation, oxygen needs to penetrate through the surface layer near step boundaries, which happens only above 800 K [15]. Using a lattice gas model, Burkhard *et al.* [10] theoretically established a temperature- and coverage-dependent O/Mo(110) phase diagram up to 0.5 ML coverage. The phase diagram exhibits a mixed phase of $p(2\times2)$ and $p(2\times1)$ structures for 0.5 ML coverage at RT, and with increasing temperature the mixed phase transforms into a single-phase region. Using density functional theory and Monte Carlo study of the O/Mo(110) system, Petrova *et al.* [16] suggested that, depending on the relative energies of the lateral interactions, it is also feasible to construct a $p(2\times1)$ oxygen-induced superstructure on the Mo(110) surface at 0.5 ML coverage. These studies indicate that by tuning the adsorption temperature, it might be possible to stabilize the oxygen-adsorbed single-phase regions, opening up the possibility for detailed structural and electronic structure characterizations for comprehensive understanding.

The electronic structure of the gas-adsorbed Mo(110) surface is also fundamentally interesting due to the fascinating phenomena observed, such as anomalous phonon softening

---

[*] krishna.menon@saha.ac.in

and Fermi surface nesting [17–19]. A hydrogen-saturated Mo(110) surface shows strong nesting behavior in its Fermi contours, in which the electron pocket grows in the area and coalesces with the corresponding contours of the second Brillouin zone [19]. With deuterium adsorption, the phonon anomaly was found to be unchanged, suggesting that the mass of the adsorbate does not influence the anomalous behavior of the surface phonons but is driven by the chemical behavior of the adsorbates. In the case of oxygen adsorption on Mo(110) using angle-resolved photoemission spectroscopy (ARPES), Dhar *et al.* [20] reported a strongly nested region for $p(2\times2)$O superstructure at 0.25 ML coverage, while the experiments by Kröger *et al.* [21] on the same system did not observe any nested regions on the Fermi surface. Thus, this controversy surrounding the Fermi surface nesting with oxygen adsorption on Mo(110) has remained unresolved for the past two decades with the appearance of mixed surface phases for higher oxygen coverages at RT. Thus, detailed electronic structure studies on single-phase regions as a function of oxygen coverage are warranted for a deep understanding of the system.

In the present work, we have systematically studied the geometric structure and electronic band dispersions of coverage-dependent oxygen-induced superstructures on the Mo(110) surface at 473 K adsorption temperature with the observation of three different single-phase superstructures. To investigate the stability of these surface structures, we have performed density functional theory (DFT) calculations for various oxygen adlayers on the Mo(110) surface. Our ARPES studies on the oxygen-adsorbed Mo(110) system confirm the absence of any Fermi surface nesting up to the saturation oxygen coverages. We have further explored the evolution of the electronic structure of the clean Mo(110) surface upon oxygen adsorption, and we observed significant changes such as opening an energy gap at the Dirac point within the valence band. Our DFT calculated band structures are also found to be in good agreement with the ARPES results, providing a fundamental understanding of the nature of interactions at the substrate-adsorbate interface.

## II. METHODS

### A. Experimental details

For the experiment, we have used a high-purity Mo(110) single crystal (MaTecK GmbH, Germany) with a miscut angle less than 0.1°. The crystal was mounted on a PTS 2000 EB/C-C sample holder (PREVAC sp. z o.o., Poland) which could be heated up to 2300 K using e-beam heating. For the surface cleaning, we followed the procedure as described in Ref. [19], consisting of several oxidation cycles: first, the crystal was heated to 1400 K and was exposed to oxygen at $1\times10^{-6}$ mbar pressure for 10 min, and then left without oxygen for 10 min. After three cycles, the crystal was flashed up to 2300 K. This process was repeated until a sharp and low background $p(1\times1)$ LEED pattern was observed. The cleanliness of the surface was further monitored by x-ray photoelectron spectroscopy (XPS) and ultraviolet photoelectron spectroscopy (UPS). Before every new experiment, it was sufficient to flash once to 2300 K to obtain a well-prepared surface. For the adsorption of oxygen on the Mo(110) surface, we back-filled the preparation chamber with high-purity oxygen (99.999%) to $1\times10^{-8}$ mbar using an ultrahigh-vacuum (UHV) leak valve, and the substrate was maintained at 473 K during adsorption. We have used Langmuir (L) as a unit of gas exposure, and 1 L is defined as an exposure of $1\times10^{-6}$ Torr of adsorbed gas for 1 s. The pressure of the chamber was measured by a Bayard-Alpert gauge while the substrate temperature was measured using a C-type thermocouple attached to the crystal.

All the measurements were carried out at RT in a UHV chamber with a base pressure better than $6\times10^{-11}$ mbar. The photoemission experiments were performed using a VG SCIENTA-R4000WAL electron energy analyzer with a two-dimensional (2D) charge-coupled device (CCD) detector. For ARPES experiments, monochromatic He I$\alpha$ (21.2 eV) and He II$\alpha$ (40.8 eV) resonance lines were used for electron excitation [22]. The total experimental energy resolutions for the ARPES measurements were better than 0.1 eV, including the thermal broadening near the $E_F$ at RT. The angular resolution was set to less than 1° at full width at half-maximum. For the Fermi surface mapping, energy scans were taken by rotating the azimuthal angle ($\phi$) by 1° each step for a fixed polar angle ($\theta$). The datasets were collected within 100° azimuthal angle window for different polar angles, and the whole Fermi surface was generated by making use of the symmetry of the Brillouin zone by stitching different polar-angle energy-scanned data.

### B. Computational details

The DFT calculations were carried out using PWSCF code, implemented in the QUANTUM ESPRESSO package [23]. The Kohn-Sham wave functions were expanded using a plane-wave basis set with a cutoff of 60 and 600 Ry for wave functions and charge densities, respectively. The exchange-correlation functional was treated using a generalized gradient approximation of Perdew-Burke-Ernzerhof (PBE) form [24]. To describe the interactions between the ionic cores and valence electrons, fully relativistic ultrasoft pseudopotentials [25] were used.

A clean Mo(110) surface was modeled using an 11-atomic-layer-thick slab with a $(1\times1)$ surface unit cell. The O atoms were adsorbed on one side of the slab only, which is commonly done in similar DFT calculations [16,26,27]. The adatoms were positioned only on one side of the slab to avoid the undesirable adatoms interaction effect across the slab [28], and it is also cost-effective in supercell calculations for the surfaces. For the oxygen-adsorbed Mo(110) surface, a nine-atomic-layer-thick slab with $p(2\times2)$ and $p(2\times1)$ surface supercells was used for 0.25 and 0.5 ML coverages, respectively. For 1 ML coverage, again a $(1\times1)$ unit cell was used for the calculation. Periodic images of the surface along the slab normal in the $z$ direction were separated by a vacuum region of width ∼16 Å to eliminate the interactions between artificially periodic images. The in-plane primitive cell lattice constant of a Mo(110) surface unit cell was determined to be 2.74 Å ($=3.16\times\sqrt{3}/2$), which is in good agreement with the experimentally obtained value of 2.72 Å as well as with earlier theoretical reports [29,30]. To acquire the ground-state

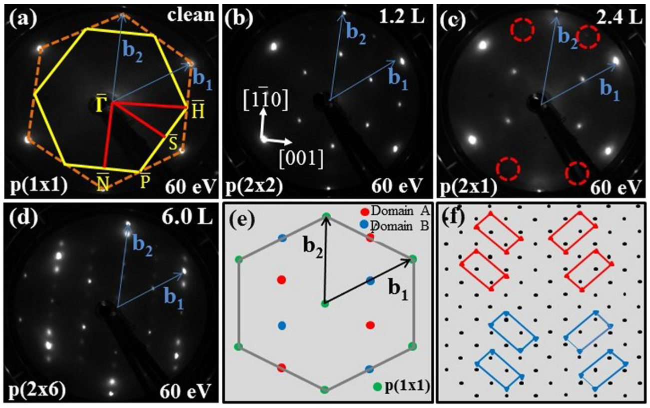

FIG. 1. (a) LEED pattern of a clean Mo(110) surface with its first Brillouin zone and high-symmetry directions. (b)–(d) LEED patterns of oxygen-induced superstructures on a Mo(110) surface for 1.2, 2.4, and 6.0 L exposure, respectively. (e) Schematic construction of a $p(2\times1)$ two equivalent domain structure. (f) Schematic model for symmetry and ground-state degeneracy for $p(2\times1)$ structure for threefold hollow coordination sites.

geometry of the system, except for the bottom three layers of the slab, the rest of the atomic layers were allowed to relax using the Broyden-Fletcher-Goldfarb-Shanno (BFGS) algorithm [31] until the forces on all the relaxed atoms were less than 0.001 Ry/Bohr. For the $1\times1$ unit cell, Brillouin-zone sampling was done by using $24\times24\times1$ Monkhorst-Pack (MP) meshes with Marzari-Vanderbilt cold smearing of width 0.002 Ry [32,33], while for larger cells the $k$-space integration points were reduced accordingly. A dipole correction term [28] is employed in our calculations to account for the asymmetry of the potential at both sides of the slab surfaces.

## III. RESULTS AND DISCUSSIONS

### A. Structural study

Adsorption of oxygen on a Mo(110) surface at an elevated temperature (473 K) was found to induce several ordered superstructures as shown in Figs. 1(a)–1(d). The $p(1\times1)$ LEED pattern of clean Mo(110) [Fig. 1(a)] reflects the $C_{2v}$ symmetry of the surface. Exposing the clean surface to 1.2 L of a molecular oxygen environment, a $p(2\times2)$ ordered LEED pattern was observed [see Fig. 1(b)]. This structure was also observed for RT adsorption at a coverage of 0.25 ML [6]. Lateral interactions between the adsorbed oxygen atoms were found to be responsible for the appearance of this $p(2\times2)$ superstructure [34,35]. For a moderately higher oxygen exposure of 2.4 L, a single-phase $p(2\times1)$ superstructure appeared in the LEED images [see Fig. 1(c)]. For this structure, the adsorbed oxygen layer contains two equivalent domains rotated by 109.5° with regard to each other, as schematically represented in Fig. 1(e). The observed LEED pattern is also consistent with the $p(2\times1)$O LEED structure obtained for the W(110) surface [36] and is different from a multidomain $p(2\times1)$ structure. For higher oxygen exposure of 6.0 L, a new single domain $p(2\times6)$ ordered LEED structure was observed, as shown in Fig. 1(d). For this surface structure, the adsorbed oxygen atoms are along $[1\bar{1}0]$, one of the unit cell vector directions.

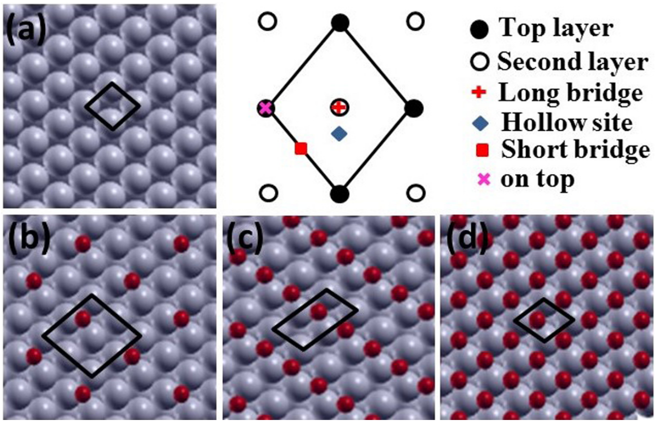

FIG. 2. (a) Top view (left panel) of the Mo (110) surface with a sketch of the surface unit cell. The four surface adsorption sites considered are represented (right panel) where the surface unit cell is sketched in black. (b)–(d) Surface structures after oxygen (red atoms) adsorption on the Mo(110) surface, referred to as (from left to right) $p(2\times2)$, $p(2\times1)$, and $p(1\times1)$ superstructures for considered coverages of 0.25, 0.5, and 1 ML, respectively. Surface unit cells used for the calculations are sketched in black.

No further evolution of the LEED patterns was observed for 12 L and above, and hence we consider this structure as the oxygen-saturated structure.

The sticking coefficient ($S$) of adatoms on a substrate surface depends on the temperature and their overlayer coverages ($\theta$). Above 200 K, the dependence of $S(\theta)$ is known to differ substantially from the Langmuir character of adsorption [15]. So, in our experiment, it is difficult to determine the absolute coverage of the adsorbed oxygen overlayer. According to the theoretical phase diagram [10], the $p(2\times2)$O structure occurs around 0.25 ML coverage while the $p(2\times1)$O structure appears between 0.35 and 0.5 ML coverage. The estimated coverage of the $p(2\times6)$O phase from the experimental exposure value and the theoretical phase diagram appears to be more than a monolayer thickness.

To investigate the structure and stability of the oxygen adlayers on the Mo(110) surface, we have considered four different high-symmetry adsorption sites: top, long-bridge, short-bridge, and threefold hollow sites [see Fig. 2(a)]. In correspondence with the observed LEED patterns, $p(2\times2)$ and $p(2\times1)$ supercells were used to represent the surface structures for 0.25 and 0.5 ML coverages, respectively. For higher oxygen coverages ($\theta > 6.0$ L) with a saturated surface structure, we have considered a $p(1\times1)$ unit cell as an approximation as the coverage is expected to be close to the monolayer coverage. The good agreement between the experimental and calculated band dispersions as shown later suggests that this approximation is a reasonable one. Further in the literature, for the case of monolayer oxygen coverages on other metallic surfaces, such as Ag(111) [26], Rh(111) [37], and Ru(0001) [27], the adsorption systems were also modeled with $(1\times1)$ surfaces. From the first-principles total energy calculations (see Table S1 in the Supplemental Material [38]), it was found that the threefold hollow site is the most stable surface adsorption position of the oxygen atom for all the coverage we considered and is consistent

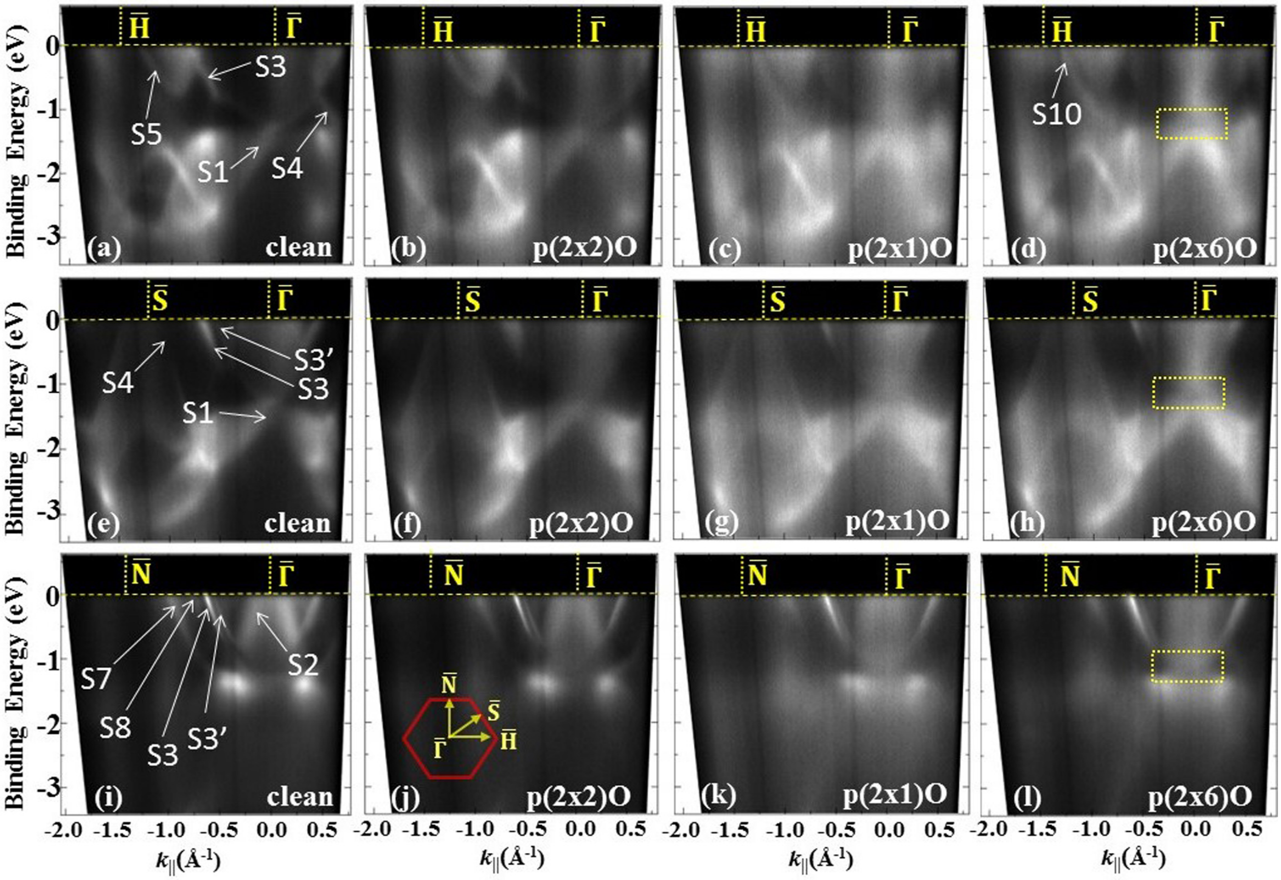

FIG. 3. ARPES spectra of a clean, $p(2\times2)$ (1.2 L), $p(2\times1)$ (2.4 L), $p(2\times6)$ (6.0 L), oxygen covered Mo(110) surface along (a)–(d) $\bar{\Gamma}\bar{H}$, (e)–(h) $\bar{\Gamma}\bar{S}$, and (i)–(l) $\bar{\Gamma}\bar{N}$ symmetry directions using He I photons. The inset schematic in (j) represents the high-symmetry directions of the first Brillouin zone of the Mo(110) surface. The surface bands near the Fermi level are labeled as S1–S10. The "rectangular box" in the ARPES spectra highlights the gap-opening region at $\bar{\Gamma}$. See text for details.

with earlier calculations [16,29]. Figures 2(b)–2(d) show the optimized geometry of the most stable structures for 0.25, 0.5, and 1.0 ML coverages, respectively. It was observed that with increasing coverage, the binding energy (BE) of oxygen atoms ($E_b^{0.25\,\mathrm{ML}} = 7.53$ eV, $E_b^{0.5\,\mathrm{ML}} = 7.41$ eV, $E_b^{1.0\,\mathrm{ML}} = 7.04$ eV) (see Table S1 in [38]) decreases significantly, indicating the repulsive interaction between the adsorbates becoming more effective with coverage [26]. A positive value of the average adsorption energy (see Table S1 in [38]) indicates that the dissociative adsorption of $O_2$ is exothermic [26,37]. As the O atoms prefer to sit on a threefold hollow site, there exist two energetically equivalent adsorption positions in a unit cell. Hence, it is possible to construct four rotationally and four translationally equivalent $p(2\times1)$ structures for 0.5 ML coverage [see Fig. 1(f)]. However, due to the energy degeneracy of the hollow adsorption sites, we only observe a rotated domain structure in our LEED experiment.

### B. Angle-resolved photoemission study

Figure 3 represents the ARPES spectra of clean and oxygen-induced superstructures on the Mo(110) surface along $\bar{\Gamma}\bar{H}$ [(a)–(d)], $\bar{\Gamma}\bar{S}$ [(e)–(h)], and $\bar{\Gamma}\bar{N}$ [(i)–(l)] symmetry directions for He I photon energy. To identify the individual bands near the Fermi level ($E_F$), we have labeled them as S1–S10, and to obtain their quantitative dispersion characteristics, line profiles at $E_F$ are plotted in Fig. 4. As the detailed band structure of the clean Mo(110) surface is well known [39], we are only briefly describing the bands that are evolving with the oxygen adsorption. S1 is an intense band observed around the zone center ($\bar{\Gamma}$) with a shape of "Λ" at about 1.35 eV below $E_F$, along the $\bar{\Gamma}\bar{H}$ [Fig. 3(a)] and $\bar{\Gamma}\bar{S}$ [Fig. 3(e)] directions. The bulk-projected band structure of the Mo(110) surface exhibits a spin-orbit-induced pseudogap region at the zone center, ∼1.25 eV below $E_F$ with a Dirac-like linear surface state within this gap region as observed for the clean W(110) surface [39,40]. Distinct identification of the surface states for Mo is more difficult than W as the spin-orbit parameter is higher for 5*d* metals in comparison with 4*d* metals, corresponding to a larger pseudogap for W (0.59 eV) than Mo (0.12 eV). However, the spin-orbit splitting of the bands is not well resolved in our experiments due to the band broadening at RT. S2 is a steep, linearly downward dispersing band observed around the zone center along the $\bar{\Gamma}\bar{N}$ direction [see Fig. 3(i)], at $k_\parallel = -0.08$ Å$^{-1}$ near $E_F$. The energy position of this S2 band does not shift with oxygen coverage, while the intensity gets reduced and the band becomes broad with increasing coverage. S3 is a highly dispersive band observed along all symmetry directions, and it crosses $E_F$ at $k_\parallel = -0.81$, $-0.62$, and $-0.59$ Å$^{-1}$ along the $\bar{\Gamma}\bar{H}$, $\bar{\Gamma}\bar{S}$, and $\bar{\Gamma}\bar{N}$ directions,

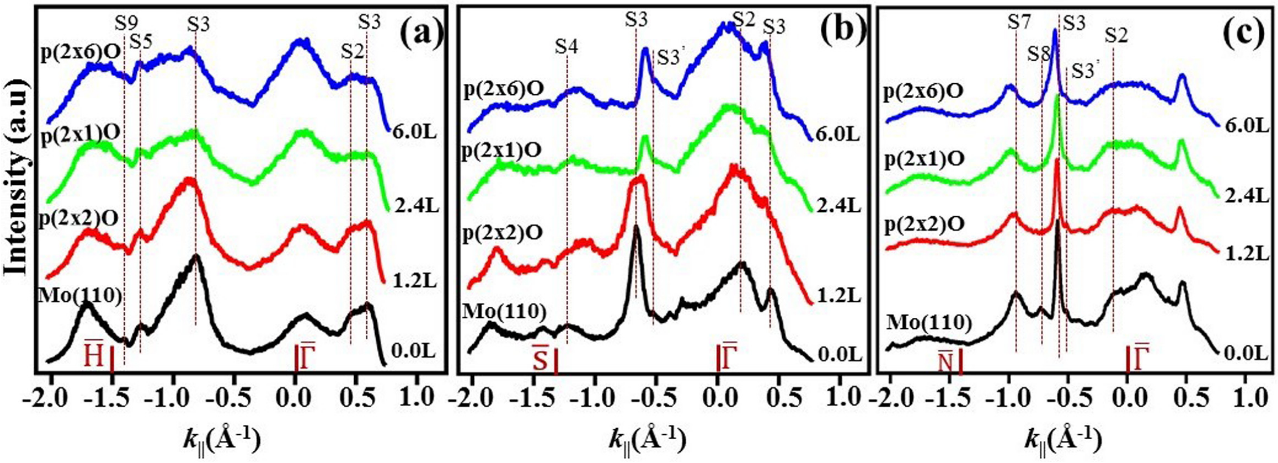

FIG. 4. Line scan spectra at $E_F$ along (a) $\bar{\Gamma}\bar{H}$, (b) $\bar{\Gamma}\bar{S}$, and (c) $\bar{\Gamma}\bar{N}$ symmetry directions of clean Mo(110), $p(2\times2)$ (1.2 L), $p(2\times1)$ (2.4 L), $p(2\times6)$ (6.0 L) oxygen covered surfaces using He I photons.

respectively. Along $\bar{\Gamma}\bar{H}$, the intensity of the S3 band gets reduced with increasing oxygen coverage, and the band gradually shifts to a higher momentum side [see Fig. 4(a)]. Along $\bar{\Gamma}\bar{N}$, the S3 band behaves in a similar way, but along $\bar{\Gamma}\bar{S}$ it is quite different. It was observed that for $p(2\times2)$O structure, the S3 band gets broader near $E_F$ [see Fig. 4(b)], and the band shifts towards the lower momentum side. With increasing coverage, the width of the S3 band gets narrower and the band shifts more towards the lower momentum side. Close to the S3 band, another band S3′ with similar dispersion behavior to that of S3 was observed clearly along the $\bar{\Gamma}\bar{N}$ direction, while along $\bar{\Gamma}\bar{S}$ the intensity of the band is quite low [see Figs. 3(e) and 3(i)]. We observe that the dispersion of the S3′ band does not change with the oxygen coverage. As per the projected band-structure calculation along the $\bar{\Gamma}\bar{S}$ direction [41], the S3′ band is inlaid into the bulk states and can be considered as a surface resonance (SR) state, while the S3 band lies in the bulk-projected band-gap region and is a surface state. This leads to a drastic decrease in the intensity of the S3′ band compared to the S3 band.

The S4 state appearing at the edge of the projected bulk band-gap region along the $\bar{\Gamma}\bar{S}$ direction builds up a boundary between the continuum bulk states and the gap region. With initial oxygen adsorption, the S4 band gets shifted to the lower momentum side, but with increasing coverage no further shift was observed [see Fig. 4(b)]. The S5 state that appears near the $\bar{H}$ point of the clean surface is found to reduce in intensity with oxygen coverage. The S7 state at $k_{\parallel} = -0.9$ Å$^{-1}$ along $\bar{\Gamma}\bar{N}$ is found to shift to higher momentum with oxygen coverage with reduced intensity but it does not disappear completely. The S8 state appearing midway to $\bar{\Gamma}\bar{N}$ is found to be very sensitive to oxygen adsorption [see Fig. 4(c)]. Another state S9 with low intensity observed near the $\bar{H}$ point is found to be prominent with He II excitation (see Fig. S1 in the Supplemental Material [38]). For the oxygen-covered surfaces, a new state S10 was observed around $\bar{H}$ at $k_{\parallel} = -1.33$ Å$^{-1}$ [see Fig. 3(d)] that becomes more pronounced with increasing oxygen coverage. At $E_F$ the S10 state gets merged with the S5 state but is distinguishable at higher BEs.

Upon oxygen adsorption on the Mo(110) surface, a gaplike opening is observed in the ARPES spectra at the zone center (marked with dotted boxes in Fig. 3). To illustrate this aspect, normal-emission spectra have been plotted for both He I and He II as shown in Fig. 5. For He I, the broad spectra between −1.2 and −1.7 eV BE of the clean Mo(110) spectra can be considered as an overlap of two spectral features arising from the SR state and the nearby bulk states (B) [21,40], while for He II only narrow SR spectra at −1.32 eV BE are apparent for clean spectra, due to the energy-dependent cross-section effects [40]. For both photon energies with increasing oxygen coverage, the intensity of the SR peak goes down rapidly with an extra peak appearing in the spectra, as indicated by arrows in Fig. 5. With increasing oxygen coverage, this oxygen-induced peak intensity increases, and the peak shifts towards the lower BE side. The measured peak separation from the SR peak is about 0.275, 0.45, and 0.625 eV for 1.2, 2.4, and 6.0 L coverages, respectively. The intensity enhancement

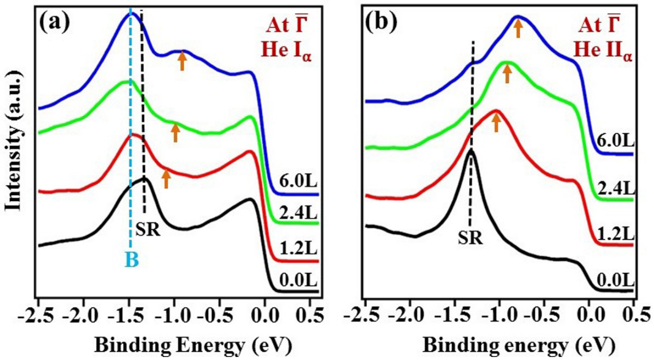

FIG. 5. Evolution of normal-emission spectra for clean, $p(2\times2)$ (1.2 L), $p(2\times1)$ (2.4 L), $p(2\times6)$ (6.0 L), oxygen covered Mo(110) surfaces. Data obtained for monochromatic (a) He I and (b) He II photons. The dotted line represents the position of the surface resonance peak. The arrows indicate the shifting of the peak with oxygen coverage. "B" and "SR" indicates the bulk and surface resonance state, respectively.

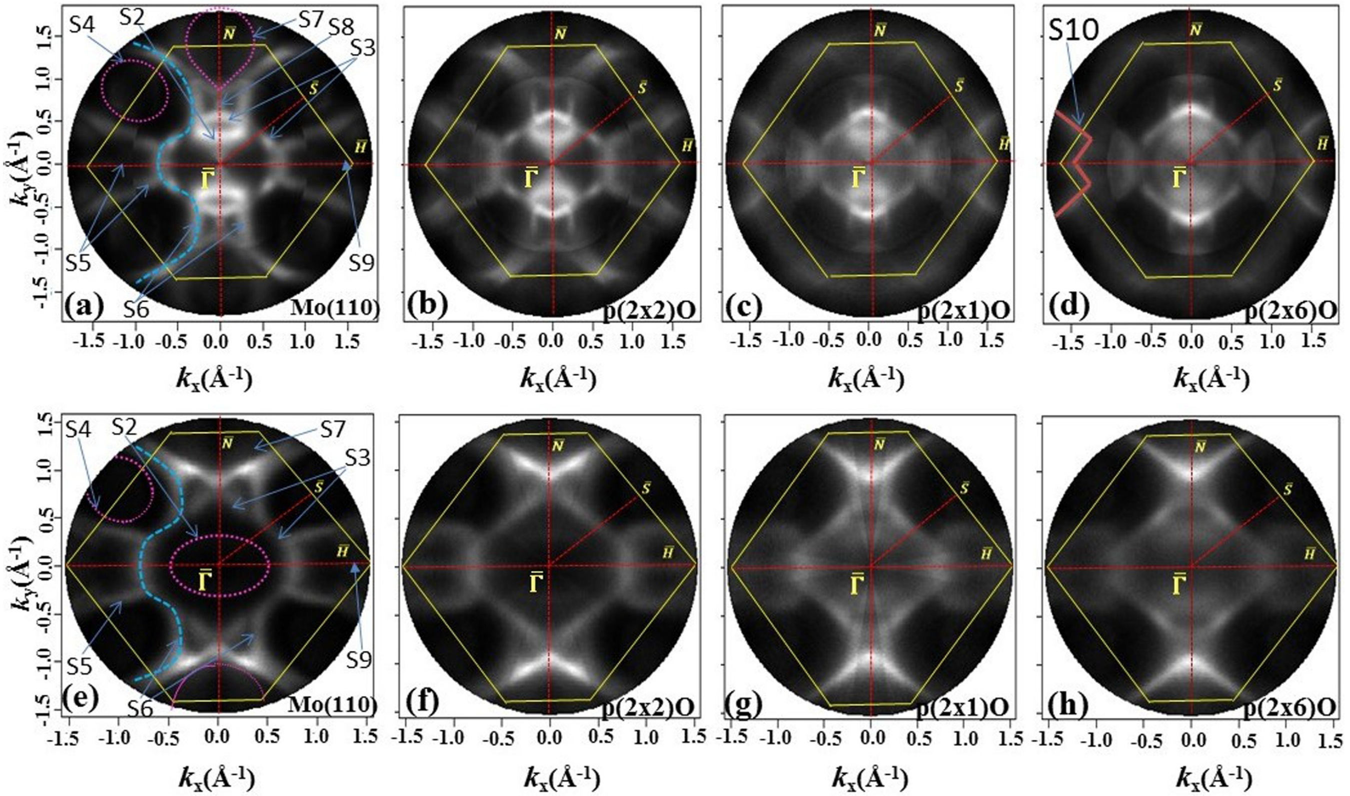

FIG. 6. Fermi surface of clean, $p(2\times2)$ (1.2 L), $p(2\times1)$ (2.4 L), $p(2\times6)$ (6.0 L), oxygen covered Mo(110) surfaces. Data obtained using (a)–(d) He I and (e)–(h) He II photons.

of the oxygen-induced peak indicates that the hybridization between the Mo 4$d$ and O 2$p$ states builds up at the interface. Adsorption of oxygen on the Mo(110) surface creates a potential barrier for the confinement of electrons leading to a gap opening at the Dirac point. This confinement can also be understood from the broadening of the ARPES bands due to increased uncertainty in the crystal momentum [42].

### C. Fermi surface mapping

To understand the evolution of the Fermi surface with oxygen coverage, we have carried out the Fermi surface mapping for clean as well as oxygen-covered Mo(110) surfaces, shown in Fig. 6 using He I [(a)–(d)] and He II [(e)–(h)] photons. The Fermi contours of the clean Mo(110) surface are found to be in good agreement with previous reports [21,44]. We observe three elliptic hole pockets centered around $\bar{\Gamma}$, $\bar{S}$, and $\bar{N}$ points and one electron pocket extended along the $\bar{\Gamma}\bar{N}$ direction $[1\bar{1}0]$, as shown in Figs. 6(a) and 6(d); the electron and hole pockets are indicated using "dashed" and "dotted" colored lines, respectively. From the ARPES spectra, we identify that S2, S4, and S7 states are responsible for the hole orbits around $\bar{\Gamma}$, $\bar{S}$, and $\bar{N}$ points, respectively. At $\bar{\Gamma}$, the "hole" orbit (S2) is inlaid in the projection of the bulk electron jack and is prominent for He II data [see Fig. 6(d)]. The electron orbit behaves as a true surface state when it is away from the symmetry line, while close to the line it is resonant with bulk states [44]. Along with surface states, various bulk-related features are also observed on the Fermi contours, which do not shows any sensitivity upon adsorption. After the adsorption of oxygen on clean Mo(110), an overall decrease in the intensities of the surface bands is observed on the Fermi surface. Even though no significant change in the electron orbit on the Fermi surface is observed with oxygen coverage, the "hole" pockets around $\bar{S}$ and $\bar{N}$ points are found to reduce its volume with coverage. On the Fermi surface, the S3 band appeared as elliptical-shaped around the zone center and formed part of the electron orbit. With increasing oxygen coverage, the elliptic feature of the S3 band gets elongated along the $\bar{\Gamma}\bar{N}$ direction and forms a more squarelike structure [see Fig. 6(d)]. Due to elongation of the S3 band, the gap between S3 and S2 bands increases with coverage along the $\bar{\Gamma}\bar{N}$ direction. On the clean surface, a horseshoe-shaped S6 band is observed along the $\bar{\Gamma}\bar{N}$ direction very close to the electron pocket contour, and these two states cannot be identified individually. After the adsorption of hydrogen [19], the electron orbit shows a significant shift from the S6 band towards higher momentum. However, with oxygen coverage, we do not observe any coalescence of the electron pocket of the first Brillouin zone with its partner in the second Brillouin zone to form a new hole pocket around the $\bar{S}$ point, as observed for H/Mo(110) [19]. Our results suggest that the Fermi surface nesting is not occurring for the O-covered Mo(110) surface up to the saturation coverage studied. After the adsorption of oxygen, a new W-shaped feature [see Fig. 6(d)] is observed around the $\bar{H}$ point on the Fermi surface and gets pronounced with increasing overlayer coverage.

First-principles calculations on a 1 ML H/Mo(110) system [45] showed that the hydrogen atoms are at a short range from the surface with an H-Mo interlayer separation (vertical

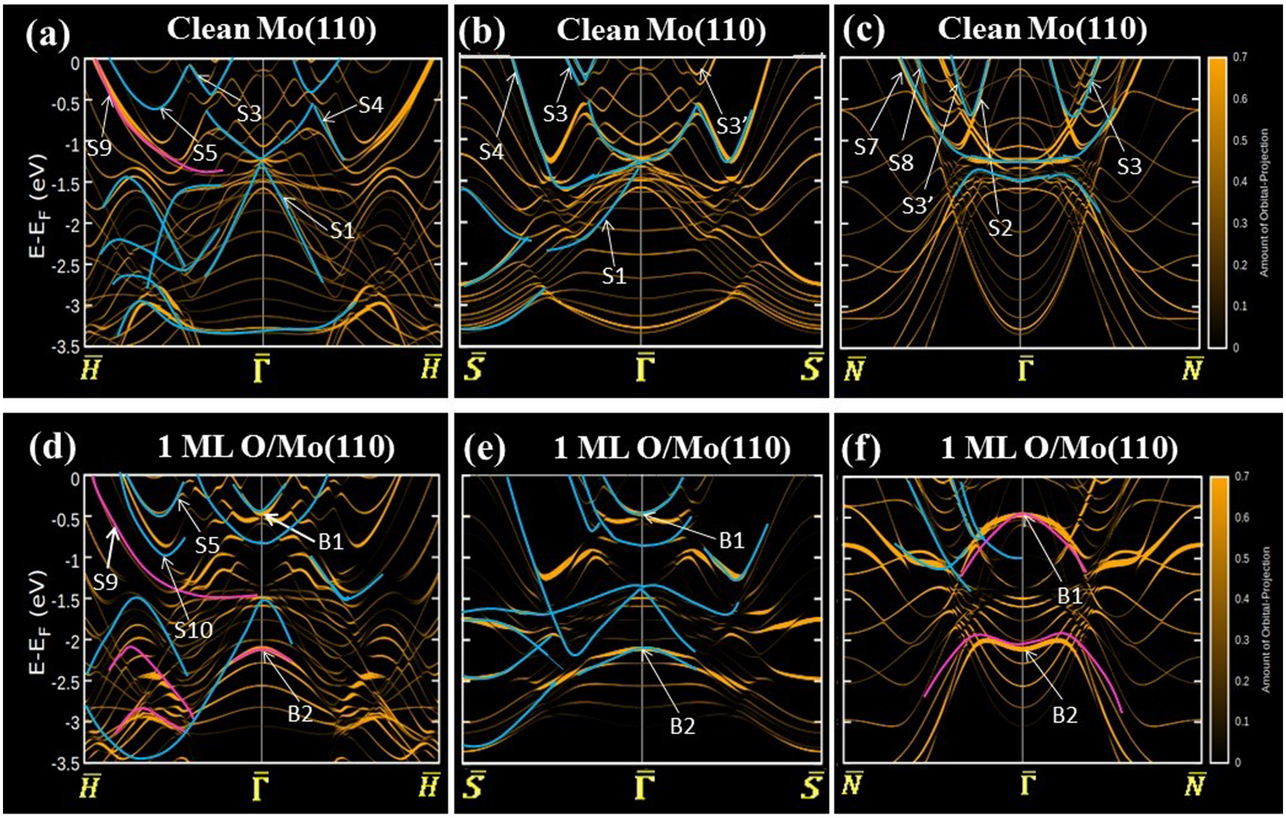

FIG. 7. The DFT calculated electronic band structure of clean Mo(110) and monolayer O/Mo(110) systems along (a) and (d) $\bar{H}$-$\bar{\Gamma}$-$\bar{H}$; (b) and (e) $\bar{S}$-$\bar{\Gamma}$-$\bar{S}$; and (c) and (f) $\bar{N}$-$\bar{\Gamma}$-$\bar{N}$ symmetry directions. The color scale represents the amount of projected spectral weight [43]. The "blue" and "pink" lines represent the experimental ARPES data obtained using He I and He II photons, respectively. See text for details.

distance) of 1.02 Å with a bond length of 1.9 Å. For the 1 ML O-Mo case, the O-Mo bond length is found to be 2.0 Å while their interlayer separation is 1.178 Å (see Table S1 in [38]), which is an increase of ∼5% and ∼15%, respectively, compared to the 1 ML H/Mo(110) system. These changes are significant and can have substantial effects on the surface potential. Thus, due to the larger interlayer distance and bond length for the O/Mo(110) system, the surface states do not feel a strong potential change by the oxygen atoms on the Mo surface as compared to hydrogen atoms. Also due to the strong lateral repulsive interactions between the oxygen atoms, the chemisorbed properties of oxygen on the Mo(110) surface differ significantly from the hydrogen adlayers.

## D. Computational results

### *1. DFT computed band structure*

We have performed DFT calculations including the spin-orbit coupling (SOC) for both the clean and oxygen-covered Mo(110) surfaces for a direct comparison with the experimental ARPES data. In Fig. 7, we show a series of computed band structures for a clean Mo(110) and a monolayer O/Mo(110) surface along the $\bar{\Gamma}\bar{H}$ [(a) and (b)], $\bar{\Gamma}\bar{S}$ [(c) and (d)], and $\bar{\Gamma}\bar{N}$ [(e)–(h)] directions of the primitive BZ. As ARPES probes the surface electronic structure, the calculated bands are projected onto the orbitals of the atoms belonging to the three outermost layers of the slab structure for a direct comparison with the experimental spectra. The color scale in Fig. 7 represents the projected spectral weight, which is an extent of the overlap between the Kohn-Sham states and the relevant atomic orbitals [43]. Here, the "orange" color represents the maximum overlap, while the "black" color represents bands with zero overlaps. For a direct comparison with the calculated band structure, the experimentally obtained band dispersions are plotted over the theoretical ones. In Fig. 7, the "blue" and "pink" lines show the experimental ARPES dispersions obtained for He I and He II photon energies, respectively. Here, we have compared the calculated dispersions of the 1 ML O/Mo(110) system with the experimental dispersions observed for the saturated oxygen coverage surface. We find good agreement between the experiment and calculations, both in dispersion characteristics as well as in their relative intensities.

The inclusion of the SOC in the calculation of the clean Mo(110) surface yields a Dirac-like surface state at the zone center, below 1.25 eV from $E_F$ (see Fig. S2 in [38]), similar to the W(110) surface [46]. Explicit orbital character analysis shows that the Dirac-like surface state is originating from the Mo-4$d$ $m_j = 1/2$ state, and upon adsorption of oxygen, this surface state vanishes and opens up a gap at this point (see Fig. S3 in [38]). The "hole pockets" (S2, S4, and S7 states) appeared around the high-symmetry points mainly occurring from Mo 5$s|1/2, \pm 1/2\rangle$ states, while the Mo 4$d|5/2, \pm 1/2\rangle$ state is responsible for the appearance of the electron pocket (see Fig. S4). As the hybridization of O-2$p$ states with Mo-4$d$ states is much stronger than Mo-5$s$ states, the intensity of the

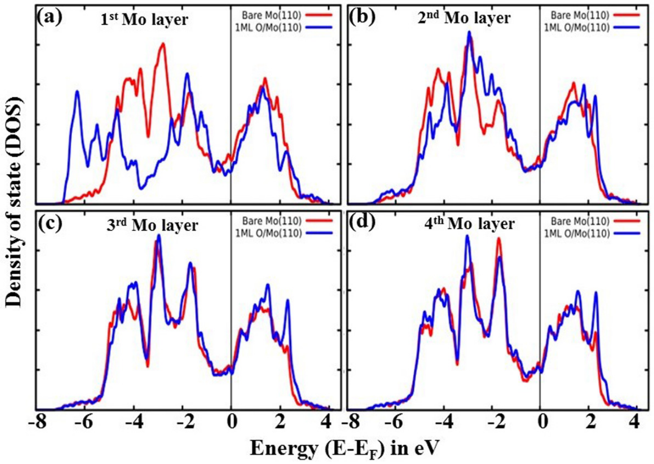

FIG. 8. Comparison between layer projected density of states (LDOS) for clean and 1 ML O/Mo(110) system. Parts (a)–(d) denote a comparison between the first, second, third, and fourth Mo layers of clean Mo(110) ("red" line) and 1 ML O/Mo(110) ("blue" line), respectively.

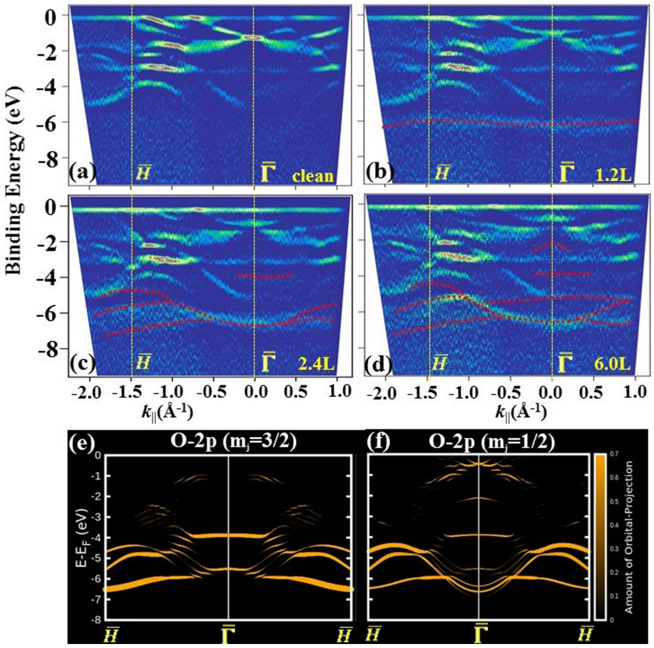

FIG. 9. Parts (a)–(d) show the second-derivative ARPES spectra of clean, $p(2\times2)$ (1.2 L), $p(2\times1)$ (2.4 L), $p(2\times6)$ (6.0 L), oxygen covered surfaces along the $\bar{\Gamma}\bar{H}$ symmetry direction using He II photons. The "red" dotted lines are for guiding the eye to compare with calculated spectra. Parts (e) and (f) show the calculated O $2p$ ($m_j = 3/2$) and O $2p$ ($m_j = 1/2$) orbitals projected band structure along the $\bar{H}$-$\bar{\Gamma}$-$\bar{H}$ symmetry direction for the top three layers, respectively.

electron pocket decays rapidly with the coverage while the hole pockets are found to persist for higher oxygen coverages. The appearance of the other states, such as S5, S9, and S10, is directly correlated with the Mo $4d|5/2, \pm3/2\rangle$, $|3/2, \pm3/2\rangle$, and $|5/2, \pm5/2\rangle$ states, respectively. For O/Mo(110) at $\bar{\Gamma}$ for $E - E_F = -0.5$ and $-2.1$ eV, two strong bands (namely, B1 and B2) are observed along all the high-symmetry directions [see Figs. 7(d)–7(f)] with different dispersion characteristics (see Fig. S6). Orbital-projected band structure reveals that these bands are originating from the hybridization of O-$2p$ $m_j = 1/2$ states with the Mo-$4d$ $m_j = 1/2$ states at the interface (see Fig. S5).

### 2. Layer-resolved density of state

To perceive the effect of oxygen adsorption on the surface of Mo(110), we have looked at the layer-projected density of states (LDOS). In Fig. 8, the layer-resolved DOS of the four successive Mo layers from the surface is shown for with and without monolayer oxygen-covered surfaces. Here, the "red" and "blue" lines show the DOS for clean and oxygen-covered surfaces, respectively. The DFT results show that the electronic states of the topmost two surface Mo layers are mostly affected by the influence of adsorbed oxygen adatoms, while the DOS of the third and fourth layers shows nearly the same behavior as the clean Mo(110) surface. So, the interaction length of the oxygen adatoms with the Mo surface extends up to about the first two layers of the surface, and the rest of the layers almost do not feel their influence. For this reason, the surface states get most affected by gas adsorption, while the bulk bands remain unaffected.

### 3. Evolution of oxygen bands

To observe the evolution of the oxygen bands, the second-derivative ARPES spectra over a wider BE range along $\bar{\Gamma}\bar{H}$ are shown in Figs. 9(a)–9(d) for He II photons. The second-derivative spectra provide a better way to visualize the weakly dispersing features [47]. Both the experimental and calculated results in Fig. 9 show that the oxygen bands are prominent below about −4.0 eV BE. Surfaces with lower oxygen coverage show a nearly nondispersive O-$2p$ band at −5.6 eV BE [see Fig. 9(b)], while with increasing coverage they become more dispersive and shift towards higher BEs due to orbital hybridization at the interface. Due to the hybridization, the width of the oxygen-induced band dispersion is found to increase with the oxygen coverage on the Mo(110) surface. For 1.2, 2.4, and 6.0 L coverages, the magnitudes of the band dispersions are about 0.1, 0.9, and 1.5 eV, respectively [see Figs. 9(b)–9(d)]. Similar symmetric band dispersions were also observed in organic molecular layers of PTCDA on Ag(110) and MBO on Cu(100) surfaces, in which the magnitude of the hybrid-state dispersions observed were about 0.23 eV [48] and 0.13 eV [49], respectively. In the case of organic molecules, mainly the unoccupied states get hybridized at the interface while the occupied states do not show significant hybridization with the substrate. In contrast, for oxygen atom adsorption we observe strong hybridization of the occupied states below the 4.0 eV BE range, and the magnitude of dispersions is higher than the case of the organic molecules. With increasing coverage, more oxygen-induced bands are visible at the high-symmetry points. The coverage-dependent evolution of the oxygen-induced bands along other high-symmetry directions is found to be similar to that along $\bar{\Gamma}\bar{H}$. Both the energy and dispersion characteristics of the oxygen bands obtained from the calculation for 1 ML coverage [see Figs. 9(e) and 9(f)] are also found to be in good agreement with the experimental dispersions of the 6.0 L coverage

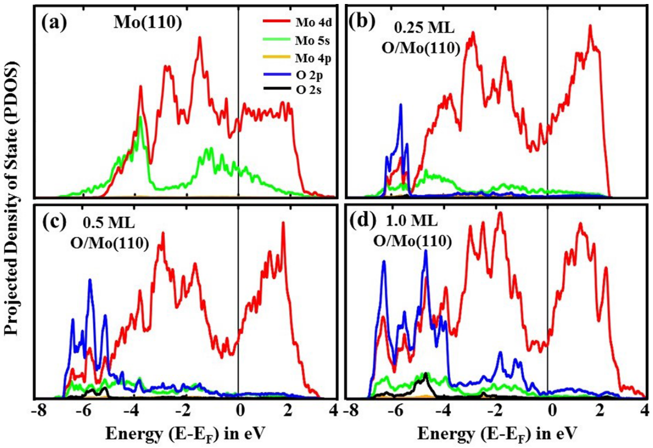

FIG. 10. Thickness-dependent projected density of states for the top two Mo layers. (a) Clean Mo(110), (b) 0.25 ML O/Mo(110) [$p(2\times2)$ structure], (c) 0.5 ML O/Mo(110) [$p(2\times1)$ structure], and (d) 1.0 ML O/Mo(110) [$p(1\times1)$ structure].

[see Fig. 9(d)]. The observed two flat bands around $\bar{\Gamma}$ at $-3.9$ and $-5.4$ eV BE in Fig. 9(d) correspond to the O-2$p$ $m_j = 3/2$ orbital, while the convex-shaped band observed at $-6.8$ eV BE mainly originates from the O-2$p$ $m_j = 1/2$ orbitals.

### 4. *Orbital-resolved projected density of state*

For insight into the hybridization of the atomic orbitals at the interface, we analyze the results of the coverage-dependent projected density of states (PDOS) in Fig. 10. Here, the band contributions for the clean Mo(110) surface are predominantly from the Mo-4$d$ states (red lines), while for the O/Mo(110) surfaces the O 2$p$ states (blue lines) also contribute significantly to the PDOS. From Fig. 10, it is evident that there is a hybridization between O-2$p$ and Mo-4$d$ orbitals at the interface, and the hybridization is getting stronger with increasing coverage. For the 0.25 ML oxygen-adsorbed surface, this hybridization is mainly below $-5.5$ eV BE [see Fig. 10(b)], while for 0.5 ML this range is extended from $-5.0$ to $-7.0$ eV [see Fig. 10(c)]. For the monolayer case, the PDOS of the O atoms shows two main regions of high electron density: bonding states below $-4.0$ eV and antibonding states in the range of $-2.0$ to 2.0 eV. In Fig. 10(d), we observe a significant amount of orbital overlap occurring in the $-4.0$ to $-7.0$ eV BE range, leading to stronger hybridization and evolution of bands, in agreement with our experimental results. Therefore, we conclude that the coverage-dependent evolution of the oxygen-induced bands is a consequence of different degrees of hybridization between Mo 4$d$ and O 2$p$ orbitals at the interface.

## IV. SUMMARY AND CONCLUSION

In summary, we have performed a detailed coverage-dependent evolution study of the geometric and electronic structure of oxygen-induced superstructures on Mo(110) surfaces using LEED, ARPES, and DFT techniques. We find that adsorption of oxygen on the Mo(110) surface at 473 K induces atomically ordered $p(2\times2)$, $p(2\times1)$, and $p(2\times6)$ superstructures for 1.2, 2.4, and >6.0 L coverages, respectively. Unlike the RT adsorption where complex surface structures are formed, the elevated temperature adsorption is shown to yield single-phase surface structures enabling a detailed and systematic study of the system. The first-principles energy calculation reveals that the dissociative adsorption of oxygen on the Mo(110) surface is exothermic, and the hollow site is the energetically most stable adsorption position for the whole coverage range considered. Energy degeneracy of the threefold hollow adsorption position is found to be responsible for the appearance of an equivalent domain structure in the LEED pattern. Coverage-dependent evolution of the binding energy of the oxygen atoms reflects that the repulsive interactions between the adsorbates are getting strengthened with increasing coverage.

The electronic band structure of clean and oxygen-adsorbed Mo(110) surfaces exhibits several highly dispersive surface states and surface resonance states near the Fermi level. After oxygen adsorption, the intensity of the surface bands decreases rapidly with a broadening of the bandwidth. Due to the confinement of the electrons, a band-gap-like opening was observed at the zone center that could be tuned with the overlayer coverage. With oxygen coverage, the surface states also get evolved in the momentum space and can be attributed to a change in surface potential due to the adsorbents. However, our photoemission results for oxygen-covered surfaces do not exhibit Fermi surface nesting behavior as observed for an H/Mo(110) system [19]. Further, a gradual buildup of a new band (with a W shape) around the $\bar{H}$ high-symmetry point with increasing coverage is observed on the Fermi contours. Due to the larger O-Mo bond length and interatomic distance (5% and 15% higher than in hydrogen, respectively) between the adsorbed layer and the substrate surface, the surface states do not feel a strong potential change, leading to an absence of the Fermi-surface nesting in oxygen-induced superstructures.

The DFT calculated band structure is found to be in good agreement with the experimental ARPES spectra. The inclusion of spin-orbit coupling induces a Dirac-like state in the occupied band at the zone center that vanishes with oxygen adsorption. Perturbation of the electronic states due to adsorption was observed only for the topmost two surface Mo layers, with the bottom layers experiencing little influence. The orbital-projected band structure shows that the hybridization between Mo-4$d$ $m_j = 1/2$ and O-2$p$ $m_j = 1/2$ orbitals at the interface is responsible for the observed evolution of the band structure. Coverage-dependent evolution of the oxygen-induced bands can be attributed to the different degrees of hybridization at the interface. The interlayer separation, bond length, and lateral repulsive interactions between the adsorbates play an important role in selective chemisorption of the surfaces for different gases.

## ACKNOWLEDGMENT

We acknowledge the Micro-Nano Initiative program of the Department of Atomic Energy (DAE), Government of India, for generous funding and support.

[1] Y. Sun, X. Hu, W. Luo, and Y. Huang, ACS Nano **5**, 7100 (2011).

[2] Y. Zhao, Y. Zhang, Z. Yang, Y. Yan, and K. Sun, Sci. Technol. Adv. Mater. **14**, 043501 (2013).

[3] J. Rajeswari, P. S. Kishore, B. Viswanathan, and T. K. Varadarajan, Electrochem. Commun. **11**, 572 (2009).

[4] T. Yunusi, C. Yang, W. Cai, F. Xiao, J. Wang, and X. Su, Ceram. Int. **39**, 3435 (2013).

[5] J. H. Song, P. Chen, S. H. Kim, G. Somorjai, R. J. Gartside, and F. M. Dautzenberg, J. Mol. Catal. A: Chem. **184**, 197 (2002).

[6] W. Witt and E. Bauer, Ber. Bunsenges. Phys. Chem. **90**, 248 (1986).

[7] T. Schroeder, J. B. Giorgi, A. Hammoudeh, N. Magg, M. Bäumer, and H.-J. Freund, Phys. Rev. B **65**, 115411 (2002).

[8] A. Santra, B. K. Min, and D. Goodman, Surf. Sci. **513**, L441 (2002).

[9] H. Over, Y. D. Kim, A. Seitsonen, S. Wendt, E. Lundgren, M. Schmid, P. Varga, A. Morgante, and G. Ertl, Science **287**, 1474 (2000).

[10] B. Dünweg, A. Milchev, and P. A. Rikvold, J. Chem. Phys. **94**, 3958 (1991).

[11] E. Bauer and H. Poppa, Thin Solid Films **121**, 159 (1984).

[12] E. Bauer and H. Poppa, Surf. Sci. **88**, 31 (1979).

[13] E. Domany, M. Schick, J. S. Walker, and R. B. Griffiths, Phys. Rev. B **18**, 2209 (1978).

[14] K. Radican, N. Berdunov, G. Manai, and I. V. Shvets, Phys. Rev. B **75**, 155434 (2007).

[15] V. Osovs' kij, D. Y. Balakyiv, Y. M. Zasimovich, J. V. Klimenko, N. Petrova, Y. G. Ptushins'kij, and Y. M. Yakovkyin, Ukrayins' kij Fyiz. Zh. (Kyiv) **54**, 200 (2009).

[16] N. V. Petrova and I. N. Yakovkin, Phys. Rev. B **76**, 205401 (2007).

[17] E. Hulpke and J. Lüdecke, Surf. Sci. **287–288**, 837 (1993).

[18] E. Hulpke and J. Lüdecke, J. Electron Spectrosc. Relat. Phenom. **64–65**, 641 (1993).

[19] J. Kröger, T. Greber, and J. Osterwalder, Phys. Rev. B **61**, 14146 (2000).

[20] S. Dhar, K. E. Smith, and S. D. Kevan, Phys. Rev. Lett. **73**, 1448 (1994).

[21] J. Kröger, T. Greber, and J. Osterwalder, Surf. Sci. **459**, 173 (2000).

[22] S. K. Mahatha and K. S. R. Menon, Curr. Sci. **98**, 759 (2010).

[23] P. Giannozzi *et al.*, J. Phys.: Condens. Matter **21**, 395502 (2009).

[24] J. P. Perdew, K. Burke, and M. Ernzerhof, Phys. Rev. Lett. **77**, 3865 (1996).

[25] D. Vanderbilt, Phys. Rev. B **41**, 7892 (1990).

[26] W.-X. Li, C. Stampfl, and M. Scheffler, Phys. Rev. B **65**, 075407 (2002).

[27] C. Stampfl and M. Scheffler, Phys. Rev. B **54**, 2868 (1996).

[28] L. Bengtsson, Phys. Rev. B **59**, 12301 (1999).

[29] Y. Zhou, X. T. Zu, J. Nie, and F. Gao, Eur. Phys. J. B **67**, 27 (2009).

[30] K. Kośmider, A. Krupski, P. Jelínek, and L. Jurczyszyn, Phys. Rev. B **80**, 115424 (2009).

[31] R. Fletcher, *Practical Methods of Optimization*, 2nd ed. (Wiley, New York, 1987).

[32] H. J. Monkhorst and J. D. Pack, Phys. Rev. B **13**, 5188 (1976).

[33] N. Marzari, D. Vanderbilt, A. De Vita, and M. C. Payne, Phys. Rev. Lett. **82**, 3296 (1999).

[34] K. Lau and W. Kohn, Surf. Sci. **75**, 69 (1978).

[35] T. L. Einstein, Crit. Rev. Solid State Mater. Sci. **7**, 261 (1978).

[36] N. Stojić, T. O. Menteş, N. Binggeli, M. A. Niño, A. Locatelli, and E. Bauer, Phys. Rev. B **81**, 115437 (2010).

[37] M. V. Ganduglia-Pirovano, K. Reuter, and M. Scheffler, Phys. Rev. B **65**, 245426 (2002).

[38] See Supplemental Material at http://link.aps.org/supplemental/10.1103/PhysRevB.106.045128 for additional figures and tables.

[39] S. Chernov, K. Medjanik, C. Tusche, D. Kutnyakhov, S. Nepijko, A. Oelsner, J. Braun, J. Minár, S. Borek, H. Ebert *et al.*, Ultramicroscopy **159**, 453 (2015).

[40] K. Jeong, R. H. Gaylord, and S. D. Kevan, Phys. Rev. B **38**, 10302 (1988).

[41] D. A. Papaconstantopoulos *et al.*, *Handbook of the Band Structure of Elemental Solids* (Springer, New York, 1986).

[42] R. A. DiDio, E. W. Plummer, and W. R. Graham, Phys. Rev. Lett. **52**, 683 (1984).

[43] J. Das, S. Biswas, K. Ulman, R. Banerjee, G. Gautam, A. K. Kundu, S. Narasimhan, and K. S. R. Menon, Phys. Rev. B **98**, 075137 (2018).

[44] K. Jeong, R. H. Gaylord, and S. D. Kevan, Phys. Rev. B **39**, 2973 (1989).

[45] P. Ferrin, S. Kandoi, A. U. Nilekar, and M. Mavrikakis, Surf. Sci. **606**, 679 (2012).

[46] H. Mirhosseini, M. Flieger, and J. Henk, New J. Phys. **15**, 033019 (2013).

[47] P. Zhang, P. Richard, T. Qian, Y.-M. Xu, X. Dai, and H. Ding, Rev. Sci. Instrum. **82**, 043712 (2011).

[48] M. Wießner, J. Ziroff, F. Forster, M. Arita, K. Shimada, P. Puschnig, A. Schöll, and F. Reinert, Nat. Commun. **4**, 1514 (2013).

[49] C. Mariani, F. Allegretti, V. Corradini, G. Contini, V. Di Castro, C. Baldacchini, and M. G. Betti, Phys. Rev. B **66**, 115407 (2002).